

# Retrieval of temperature and humidity profiles from ground-based high-resolution infrared observations using an adaptive fast iterative algorithm

Wei Huang<sup>1</sup>, Lei Liu<sup>2</sup>, Bin Yang<sup>1</sup>, Shuai Hu<sup>2</sup>, Wanying Yang<sup>2</sup>, Zhenfeng Li<sup>1</sup>, Wantong Li<sup>3</sup>, Xiaofan Yang<sup>1</sup>

<sup>1</sup>The State Key Laboratory of Complex Electromagnetic Environment Effects on Electronic and Information System, Luoyang 471003, China

<sup>2</sup>College of Meteorology and Oceanography, National University of Defense Technology, Changsha 410073, China

<sup>3</sup>Tianjin Meteorological Radar Research & Trial Centre, Tianjin 300061, China

Correspondence to: Lei Liu (liulei17c@nudt.edu.cn)

**Abstract.** Various retrieval algorithms have been developed for retrieving temperature and water vapor profiles from the Atmospheric Emitted Radiance Interferometer (AERI) observations. The physical retrieval algorithm, named AERI Optimal Estimation (AERIOe), outperforms other retrieval algorithms in many aspects except the retrieval time, which is significantly increased due to the complex radiative transfer process. The calculation of the Jacobian matrix is the most computationally intensive step of the physical retrieval algorithm. Interestingly, an analysis of the change in AERI observations' information content with respect to Jacobians revealed that the AERIOe algorithm's performance presents negligible dependence on these metrics. Thus, the Jacobian matrix could remain unchanged when the variation in the atmospheric state is small in the retrieval process to reduce the most time-consuming computation. On the basis of the above findings, a fast physical-iterative retrieval algorithm was proposed by adaptively recalculating Jacobians in keeping with the changes in the atmospheric state. Experiments with synthetic observations demonstrate that the proposed method experiences an average reduction in retrieval time by an impressive 59% compared to the original AERIOe algorithm while achieving maximum root-mean-square errors of less than 0.95 K and 0.22 log (ppmv) for heights below 3 km for the temperature and water vapor profile, respectively. Further analyses revealed that the fast retrieval algorithm reached an acceptable convergence rate of 98.7%, marginally lower than AERIOe's 99.9% convergence rate for the 826 cases used in this study.

## 1 Introduction

High-quality atmospheric profiles are required for many endeavors, including radiative transfer, cloud process research, and assimilation into mesoscale models to improve forecasts (Turner et al., 2000). The accuracy of the initial field provided by observation networks is becoming a key factor restricting the skill of numerical weather prediction (NWP) models (Romine et al., 2013; Li et al., 2016). The existing observation networks are insufficient to meet the needs of convective scale

Deleted: A

Deleted: of

Deleted: of AERIOe algorithm

Deleted: had

Deleted: little

Deleted: Jacobians

Deleted: of

Deleted:

Deleted:

Deleted: of

Deleted: The performance of the algorithm was evaluated using synthetic ground-based infrared spectra observations.

Deleted: The retrieval speed was significantly improved compared with the original AERIOe algorithm under the condition that the parameters of the computing platform remain unchanged, resulting in an average retrieval time reduction by 58.82%. The retrieval results of the fast retrieval model are comparable to that of AERIOe, with maximum root-mean-square errors of less than 0.95 K and 0.22 log (ppmv) for heights below 3 km for the temperature and water vapor, respectively. Results based on synthetic observations

Deleted: 6

Deleted: which is slightly

Deleted: the

Deleted: 88

Deleted: of AERIOe

Deleted:

Deleted: profiles of

Deleted: constituents

30 numerical weather prediction systems, especially in the prediction of convection initiation convective processes ([Kain et al., 2013](#); [Wagner et al., 2019](#); [Geerts et al., 2018](#)). As the spatiotemporal resolution is too coarse, radiosonde profiles cannot capture the atmospheric phenomena in detail. ~~Satellite-borne instruments are able to provide denser sounding coverage than ground-based balloon radiosonde observations. However, satellite retrievals remain insufficient to resolve the structure within the planetary boundary layer (PBL), as the weighting functions of satellite-borne observations peak above the PBL.~~ A promising solution is ~~ground-based thermal infrared spectrometers that measure downwelling spectral infrared radiance, which show good skill at retrieving the temperature and humidity profiles of the PBL.~~

Deleted: Space-based detection equipment observes atmospheric upwelling radiance, which demonstrates some drawbacks in the detection of the planetary boundary layer (PBL) owing to the influence of the cloud layer or the underlying surface.

Deleted: the

The commonly used ground-based infrared hyperspectral equipment mainly includes Fourier Transform Infrared (FTIR) instruments of the Karlsruhe Institute of Technology deployed in the Detection of Atmospheric Composition Change (NDACC) ([De Mazière et al., 2018](#)) and AERI developed by the University of Wisconsin Space Science and Engineering Center (UW-SSEC) deployed in the Atmospheric Radiation Measurement (ARM) program ([Knuteson et al., 2004](#)). The FTIR instrument observes near-infrared and mid-infrared high-resolution solar spectra, which are mainly used to retrieve water vapor ([Schneider et al., 2006a, b](#); [Schneider and Hase, 2009](#)), water isotopologues ([Schneider et al., 2006a](#); [Barthlott et al., 2017](#)) and various trace gas ([Gardiner et al., 2008](#); [Kiel et al., 2016](#); [Zhou et al., 2018](#); [Yin et al., 2020](#); [Yin et al., 2021a](#); [Yin et al., 2021b](#); [Viatte et al., 2014](#)) profiles or total columns. The spectral region of AERI covers the range of 520-3000  $\text{cm}^{-1}$ , containing a 15  $\mu\text{m}$  absorption band of  $\text{CO}_2$  commonly used for the retrieval of temperature profiles, which makes it more advantageous in detecting thermodynamic profiles ([Rowe et al., 2006](#)). Specific retrieval algorithms, capable of being divided into statistical retrieval algorithms and physical retrieval algorithms as per different principles, are required to extract large amounts of information on the ~~retrieved~~ atmospheric profiles from infrared hyperspectral radiance data. ~~Physical retrieval algorithms utilize the radiative transfer process and the iterative optimization strategy, which exhibit higher retrieval accuracy compared to the statistical retrieval algorithm,~~ ([Yang and Min, 2018](#); [Cimini et al., 2010](#)). Two physical retrieval algorithms, named AERIprof ([Smith et al., 1999](#); [Feltz et al., 1998](#)) and AERIOe ([Turner and Löhnert, 2014](#); [Turner and Blumberg, 2019](#); [Turner and Löhnert, 2021](#)), ~~have~~ been successively adopted in AERI equipment to derive thermodynamic profiles. Based on the "onion peeling" ~~technique,~~ ~~AERIprof~~ ~~adjusts~~ the first-guess profile from bottom to top with the iterative algorithm to minimize the difference between the calculated and observed radiation. Given that ~~AERIprof~~ only needs to calculate the diagonal elements in the Jacobian matrix, its retrieval speed is faster than that of the optimal estimation method ([Rodgers, 2000](#)).

Deleted: The assimilation of ground-based infrared hyperspectral data can significantly improve the abilities of convective scale prediction systems for convection initiation ([Coniglio et al., 2019](#); [Hu et al., 2019](#)).

Deleted: required

Deleted: rich

Formatted: Font color: Auto

Deleted: The physical retrieval algorithm includes the radiative transfer process

Deleted: which enables it to provide thermodynamic profiles with higher accuracy than the statistical retrieval algorithm

Deleted: has

Deleted: the

Deleted: algorithm

Deleted: the former

Deleted: is used to

Deleted: the algorithm

Deleted: (OEM)

55 However, the AERIprof algorithm has several significant drawbacks, such as its high dependence on the first-guess profile and inability to provide uncertainty estimates for retrieval results ([Turner and Löhnert, 2014](#); [Blumberg et al., 2017](#); [Blumberg et al., 2015](#)). The limitations of AERIprof could be overcome by the AERIOe optimal-estimation retrieval

60 algorithm, which was designed as an alternative to the previous physical algorithm. One of the important improvements  
remains to reduce the dependence on the first-guess profile by introducing regularization parameters in the AERIOe  
algorithm to balance the observation and the prior information. However, to achieve good stability and accuracy, AERIOe  
adheres to a strategy of progressively setting regularization parameters from higher to lower values, leading to a minimum of  
seven iterations for convergence. Additionally, the Jacobian matrix is recalculated for each iteration due to the dependence  
65 on the current state vector, which significantly increases the amount of calculation and results in a high retrieval time.

The aim of this study is to accelerate the retrieval speed of AERIOe. In Sect. 3, an investigation into the information  
content of AERI observations concerning Jacobians revealed that the performance of the AERIOe algorithm exhibits  
marginal dependence on these matrices. Motivated by this finding, a fast physical-iterative retrieval method, henceforth  
called Fast AERIOe, is proposed to address the limitation of the long retrieval time of AERIOe by adaptively recalculating  
Jacobians without manual intervention. By this means, the retrieval speed of AERIOe can be improved due to the reduction  
70 in computation amount. In this study, only temperature and water vapor profiles are retrieved from Fast AERIOe, and cases  
of cloudy situations will be addressed in future work. Finally, the retrieval time, convergence characteristics and accuracy of  
the new algorithm are presented in Sect. 4.

## 2 Data

75 The data used in the study are from the ARM program supported by the U.S. Department of Energy, which aims to  
quantitatively study the atmospheric radiation budget and develop and verify the parameterization scheme of the numerical  
model ([Revercomb et al., 2003](#); [Ellingson et al., 2016](#)). This program mainly focuses on the long-term observation of  
atmospheric states and radiative fluxes, providing information to researchers around the world to inform and validate  
predictive models of climate and weather. We use data collected at the Southern Great Plain (SGP) site, which is located at  
80 36.61 ° N and 149.88 ° W, near Lamont, Oklahoma, USA ([Sisterson et al., 2016](#)). These data mainly include ground-based  
infrared spectra obtained by AERI and radiosonde profiles, with the former used to retrieve the temperature and water vapor  
profiles and the latter mainly used to evaluate the accuracy of the retrieval results.

### 2.1 AERI

85 AERI can continuously receive downwelling atmospheric infrared radiance from 3.3-19.2  $\mu\text{m}$  ( $520\text{-}3000\text{ cm}^{-1}$ ) with a  
spectral resolution better than  $1\text{ cm}^{-1}$ , among which the infrared radiation of the  $520\text{-}1800\text{ cm}^{-1}$  band is obtained by the  
mercury cadmium telluride (HgCdTe) detector, and the  $1800\text{-}3020\text{ cm}^{-1}$  band is obtained by the indiumantimonide (InSb)  
detector. The AERI front-end optics include a scene mirror and two calibrated blackbodies, one of which changes with the

Deleted: The AERIOe algorithm sets regularization parameters as fixed values from large to small to achieve good stability and accuracy, which makes the algorithm require at least 7 iterations. T

Deleted: should be

Deleted:

Deleted: A

Deleted: The original AERIOe algorithm was modified to allow Jacobians to be recalculated adaptively without manual intervention by monitoring the change of atmospheric state.

Deleted: Thus

Deleted: of

Deleted: handled

Deleted: a

Deleted: Last

Deleted: using radiosonde observations at the same station

Deleted:

Deleted:

Deleted: will

temperature of the surrounding environment, while the other ~~is maintained~~ at a fixed temperature (60 °C). AERI achieved a calibration accuracy of better than 1% by viewing two high-precision blackbodies and a nonlinearity correction for the detectors (Knuteson et al., 2004). The temporal resolution of the AERI standard remains approximately 8 minutes, including a 3-minute sky dwell period and the subsequent observation of the two blackbodies.

**Table 1.** Spectral regions used for retrieving temperature and water vapor profiles in the AERIOe algorithm

Temperature	Water Vapor
612-618 cm <sup>-1</sup>	538-588 cm <sup>-1</sup>
624-660 cm <sup>-1</sup>	
674-713 cm <sup>-1</sup>	

AERI has many observation channels, including not only temperature and humidity profile information but also trace gas information such as ozone, methane, and ~~random error. To avoid contributions to the downwelling radiance by other~~ gases, appropriate channels ~~that are primarily sensitive to the retrieved profiles must be selected.~~ The spectral regions used in the ~~study~~ are consistent with AERIOe v1.2, which used only the 538–588 cm<sup>-1</sup> band for water vapor profiling to exclude scattering effects from clouds (Turner and Blumberg, 2019). ~~The specific wavenumbers used to perform the retrieval are~~ shown in Table 1, among which the spectral region used for temperature retrieval includes 167 channels, and the water vapor includes 104 channels.

## 2.2 Radiosonde data

Radiosondes have been used for decades to provide humidity, temperature and wind profiles throughout the troposphere ~~and~~ ~~are~~ considered to be the most accurate means to detect the vertical structure of the atmosphere. It is often used to evaluate the accuracy of other ~~ground-based profilers.~~ Located 150 m to the north of the AERI equipment, the closer radiosonde release point can ensure the comparability of radiosonde profiles and AERI retrieval results (Wakefield et al., 2021). The radiosonde data at the SGP site were obtained by Vaisala RS92 since 2002 (Turner et al., 2016), including temperature, humidity, pressure, wind direction and wind speed. It was regularly launched four times a day at 05:30 UTC, 11:30 UTC, 17:30 UTC and 23:30 UTC.

We collected radiosonde profiles and AERI radiation data ~~from~~ 2012, screening 826 groups of qualified data samples through quality control, spatiotemporal matching, and clear sky recognition. ~~A synthetic dataset of simulated AERI spectra~~ corresponding to 826 sets of radiosonde profiles ~~was produced~~ using the line-by-line radiative transfer model (LBLRTM), with parameter settings consistent with Sect. 3.1.

Deleted: s

Deleted: redundant

Deleted: data

Deleted: Therefore,

Deleted: must be selected

Deleted: when retrieving temperature and humidity profiles. The retrieval of humidity profiles generally adopts water vapor-sensitive channels, and the temperature profiles could be retrieved from channels sensitive to a uniformly mixed gas (such as CO<sub>2</sub>).

Deleted: retrieval process

Deleted: S

Deleted:

Deleted: , which is

Deleted: detection methods

Deleted: of

Deleted: On the basis of the above datasets, we calculated the

Deleted: um

### 3 Methodology

#### 3.1 Retrieval configuration

The AERIOe algorithm, based upon the optimal estimation method, iteratively searches for the atmospheric state that most conforms to the observation and prior constraints.

$$\mathbf{X}_{n+1} = \mathbf{X}_a + (\mathbf{K}_n^T \mathbf{S}_e^{-1} \mathbf{K}_n + \gamma \mathbf{S}_a^{-1})^{-1} \mathbf{K}_n^T \mathbf{S}_e^{-1} \times (\mathbf{Y}^m - F(\mathbf{X}_n) + \mathbf{K}_n (\mathbf{X}_n - \mathbf{X}_a)), \quad (1)$$

Here,  $\mathbf{X}$  is the profile of the atmospheric state to be retrieved,  $\mathbf{X}_a$  is the prior profile of the atmosphere,  $\mathbf{S}_a$  is the a priori covariance matrix,  $\mathbf{Y}^m$  is the observed radiance vector,  $F(\mathbf{X})$  is the computed radiance for  $\mathbf{X}$ ,  $\mathbf{S}_e$  is the observation error covariance matrix, and  $n$  denotes the iteration number. The superscripts  $T$  and  $-1$  imply the matrix transpose and inverse, respectively.

To improve the stability of the retrieval algorithm, the regularization parameter  $\gamma$  was introduced in Formula (1), which is set as fixed values from large to small ([1000, 300, 100, 30, 10, 3, 10, 1]). As  $\gamma$  decreases with iterations, more observation information is introduced to improve the retrieval accuracy. Iterations are continued until  $\gamma$  decreases to 1 and the following convergence criterion is satisfied.

$$\text{convergence\_index} = \frac{(\mathbf{X}_n - \mathbf{X}_{n+1})^T \mathbf{S}_e^{-1} (\mathbf{X}_n - \mathbf{X}_{n+1})}{N} \leq 1, \quad (2)$$

$N$  represents the dimension of the retrieved atmospheric state vector.

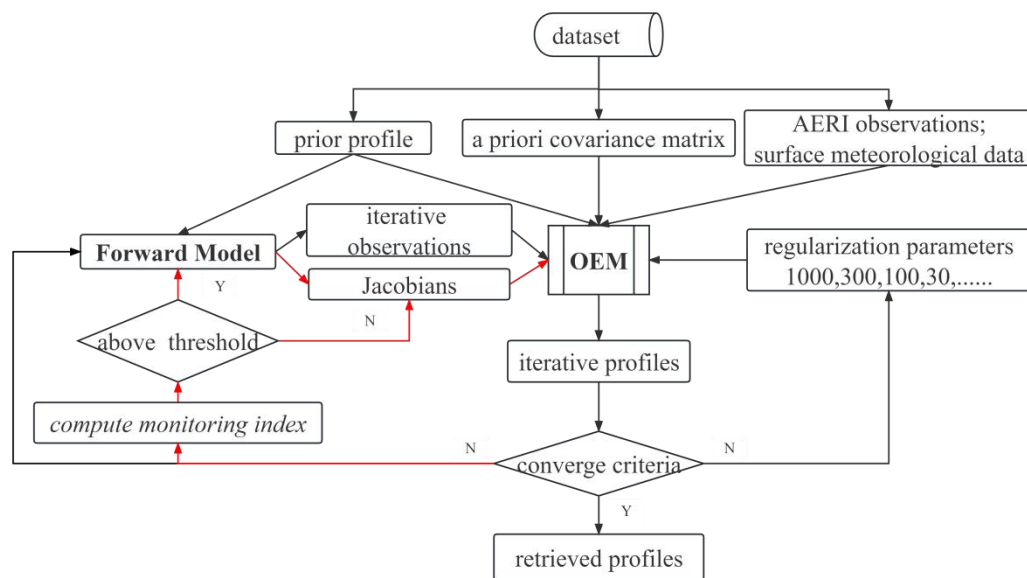


**Figure 1.** Flowchart of the Fast AERIOe retrieval process. Note that the red line indicates the Jacobian updating process. The iterative profiles and observations are defined as temperature and water vapor profiles at iteration  $n$  and computed radiance for  $\mathbf{X}_n$ , respectively.

The monitoring index is used to derive the variations in  $\mathbf{X}_n$ .

Note that  $\mathbf{K}$  depends on  $\mathbf{X}$  used for estimating the Jacobian, which means that  $\mathbf{K}$  must be recomputed for every iteration step. The updating of the Jacobians in the above retrieval process requires the calculation of the optical thickness or radiance

(intensity) with respect to the elements of  $\mathbf{X}$ , at each height, which might be computationally expensive depending on the lengths of  $\mathbf{X}$  and  $\mathbf{Y}^m$  (Maahn et al., 2020). Owing to the constraints of  $\gamma$ , the decrease in the difference between the

Deleted: different atmospheric constituents

Deleted: of

135 simulated and observed radiation is not very much in the adjustment of individual iterations to the retrieval profile. At this time, the change in the Jacobian calculated as per the iteration profile is negligible. Backed by the above analysis, a fast iterative algorithm called Fast AERIOe is proposed on the basis of the AERIOe algorithm. The flowchart of Fast AERIOe is

shown in Fig. 1. Most of the configurations are consistent with AERIOe described by Turner and Löhnert (2014), except for

Deleted: ,

some modifications highlighted as follows:

Deleted: m

140 a. Atmospheric configurations: The height grid of  $\mathbf{X}$  is consistent with AERIOe, but the maximum retrieval height is limited to 3 km. This is done because the variations in  $\mathbf{K}$  above 3 km are negligible because most of the information in the

Deleted: a

AERI spectrum lies in the lowest 2 km of the atmosphere for temperature and water vapor profiles (Turner and Löhnert, 2014). The cloud properties were excluded from the state vector  $\mathbf{X}$ , which is beyond the scope of this study. The

Deleted: of

Deleted: is

corresponding prior profile  $\mathbf{X}_a$  and the prior covariance matrices represented by  $\mathbf{S}_a$  are modified to be consistent with  $\mathbf{X}$ .

Deleted: due to the fact that

145 b. Observational vector  $\mathbf{Y}$ : Spectral regions that are sensitive to cloud properties were removed from the observational vector  $\mathbf{Y}$  to be consistent with state vector  $\mathbf{X}$ . Furthermore, additional observations, including surface temperature and water vapor, were incorporated into the observation vector; details are described by Turner and Blumberg (2019).

Deleted: i

Deleted: i

Deleted: o

c. Jacobian matrix  $\mathbf{K}$ :  $\mathbf{K}$  is derived from LBLRTM, which is the same as AERIOe except for version (12.8 instead of 12.1). Another modification is that  $\mathbf{K}$  is not recomputed to improve the retrieval speed of the algorithm when the variations

Deleted: the

Deleted: ,

150 in the iterative profile  $\mathbf{X}_n$  are small.

Deleted:

### 3.2 Adaptive recalculation of Jacobian

Deleted: the

Deleted: of

The method to reduce the calculation of  $\mathbf{K}$  is the key to speeding up the AERIOe algorithm. The Jacobians are dependent on the atmospheric state, which means that  $\mathbf{K}$  must be recalculated for every iteration step. The question arises as to under what

Deleted: is

Deleted:

circumstances  $\mathbf{K}$  does not need to be recalculated. Therefore, the dependence of the retrieval capability on Jacobians must be analyzed and indicators that reflect the changes in Jacobians should be determined to determine whether  $\mathbf{K}$  is recalculated or

Deleted: constituents

not.

Deleted: of

Deleted: f

#### 3.2.1 Quantification of algorithm retrieval capability

Deleted: igured out

The retrieval accuracy of the atmospheric profile depends on the amount of atmospheric information in the hyperspectral data. Shannon Information Content ( $SIC$ ) and Degrees of Freedom for Signal ( $DFS$ ), as important indicators to describe the

Formatted: Font: Not Bold

Deleted:

160 effective information contained in hyperspectral data (Rodgers, 1998), can quantitatively describe the detector's retrieval ability for specific atmospheric **profile**. *SIC* represents the reduction **in** uncertainty in the retrieved profiles contributed by the observation, with the calculation formula shown in (3). *DFS* provides the number of independent pieces of information contained in the measured radiation, with the calculation formula shown in (4).

Deleted: constituents

Deleted: of

$$SIC = \frac{1}{2} \ln \det(\hat{\mathbf{S}}^{-1} \mathbf{S}_a), \quad (3)$$

Deleted:

165 
$$DFS = \text{Trace}(\mathbf{B}^{-1} \mathbf{K}_n^T \mathbf{S}_e^{-1} \mathbf{K}_n), \quad (4)$$

Here,  $\hat{\mathbf{S}}$  is the posterior error covariance matrix, also known as the analysis error covariance matrix. Its diagonal element is the standard deviation of the retrieval error, with the calculation formula  $\hat{\mathbf{S}}$  as follows:

$$\hat{\mathbf{S}} = \mathbf{B}^{-1} (\mathbf{K}^T \mathbf{S}_e^{-1} \mathbf{K} + \gamma^2 \mathbf{S}_a^{-1}) \mathbf{B}^{-1}, \quad (5)$$

Among which,

170 
$$\mathbf{B} = (\gamma \mathbf{S}_a^{-1} + \mathbf{K}_n^T \mathbf{S}_e^{-1} \mathbf{K}_n), \quad (6)$$

### 3.2.2 Analysis of the dependence of AERIOe on Jacobians

It can be seen from equations (3) and (4) that *SIC* and *DFS* are determined by  $\mathbf{S}_e$ ,  $\mathbf{S}_a$ ,  $\mathbf{K}$  and  $\gamma$ . However,  $\mathbf{S}_a$  and  $\mathbf{S}_e$  remain unchanged during retrieval, which makes *SIC* and *DFS* change with iteration due to variations in  $\gamma$  and  $\mathbf{K}$ . As  $\gamma$  drops to 1 at the final iteration, the values of *SIC* and *DFS* are only dependent on  $\mathbf{K}$ . Owing to the difficulty of quantifying the change in the two-dimensional Jacobian caused by the iteration profiles, a monitoring index, henceforth called *K\_Index*, is designed and used to characterize the change **in** the profiles at various iterations. The calculation of *K\_Index* comes from the convergence criteria *convergence\_index*, which contains not only the difference between the iteration profiles but also the posterior dominated by Jacobian. The introduced *K\_Index* should reflect the changes in the temperature and humidity profile, which means that the influence of the Jacobian should be excluded. Then, the *convergence\_index* was degenerated into the

Deleted: of

180 *K\_Index* as follows.

$$K\_Index = \frac{(\mathbf{X}_n - \mathbf{X}_{n+1})^T (\mathbf{X}_n - \mathbf{X}_{n+1})}{N}, \quad (7)$$

Deleted:  $K\_Index = \frac{(\mathbf{X}_n - \mathbf{X}_n)^T (\mathbf{X}_n - \mathbf{X}_n)}{N}$

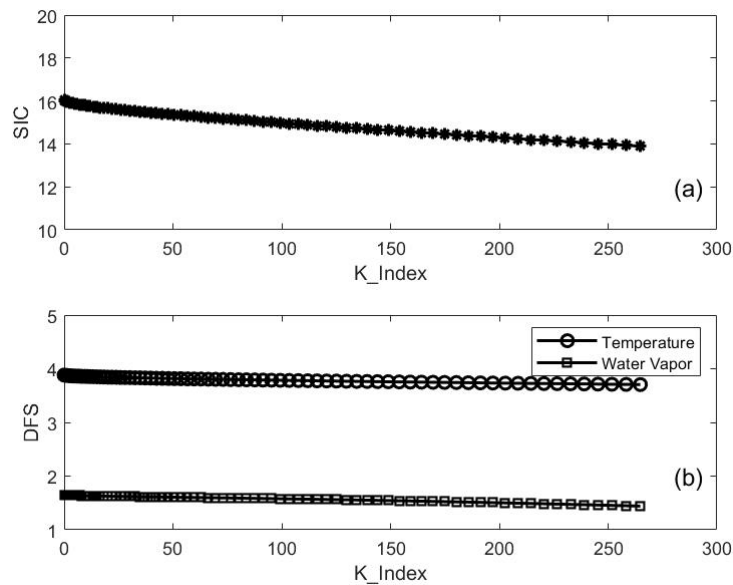


**Figure 2.** (a) The change in  $SIC$  as a function of  $K\_Index$ . (b) The change in  $DFS$  as a function of  $K\_Index$  for temperature (unfilled circles) and water vapor (open squares).

The values of  $K\_Index$  in Fig. 2, which cover most of the  $K\_Index$  during the AERIOe retrieval process (ranging from 0 to 260, see Fig. 3), were obtained by multiplying the prior profile by different scale factors. The atmosphere-dependent  $\mathbf{K}$  values were computed by the LBLRTM with the prior profiles above, and  $SIC$  and  $DFS$  were calculated using equations (3) and (4) with different Jacobians, respectively. Both  $SIC$  and  $DFS$  change slowly with  $K\_Index$  as shown in Fig. 2, with the variation of  $SIC$  within 13% (from 13.9 to 16.1) and  $DFS$  within 4% (from 3.7 to 3.9) for temperature and within 13% (from 1.4 to 1.7) for water vapor, which demonstrates that  $SIC$  and  $DFS$  remain almost unchanged on the condition that the value of  $K\_Index$  is small. This provides an effective means to improve the retrieval speed of AERIOe by recalculating  $\mathbf{K}$  selectively when  $\mathbf{X}$  is not changing much or  $K\_Index$  is small. This could be achieved by comparing the value of  $K\_Index$  with its threshold at each iteration to determine whether  $\mathbf{K}$  is recalculated or not.

### 3.2.3 Determination of the $K\_Index$ threshold

The selection of the threshold for  $K\_Index$  is very important for the Fast AERIOe algorithm. If the threshold remains too large, too many Jacobians will stop updating, resulting in a decline in retrieval accuracy or even nonconvergence of the retrieval process; when the threshold value remains too small, most Jacobians need to be recalculated, which cannot effectively shorten the retrieval time.

Deleted: of  
Deleted: with  
Deleted: of  
Deleted: with  
Deleted: , respectively  
Deleted: s  
Deleted: ed  
Deleted:  
Deleted: .46  
Deleted: 8  
Deleted: 05  
Deleted: ,  
Deleted: .38  
Deleted: 1  
Deleted: to  
Deleted: 88  
Deleted: 2.7  
Deleted: 4  
Deleted: 65  
Deleted: :  
Deleted: i  
Deleted: the  
Deleted: of  
Deleted: the  
Deleted: -  
Deleted: while



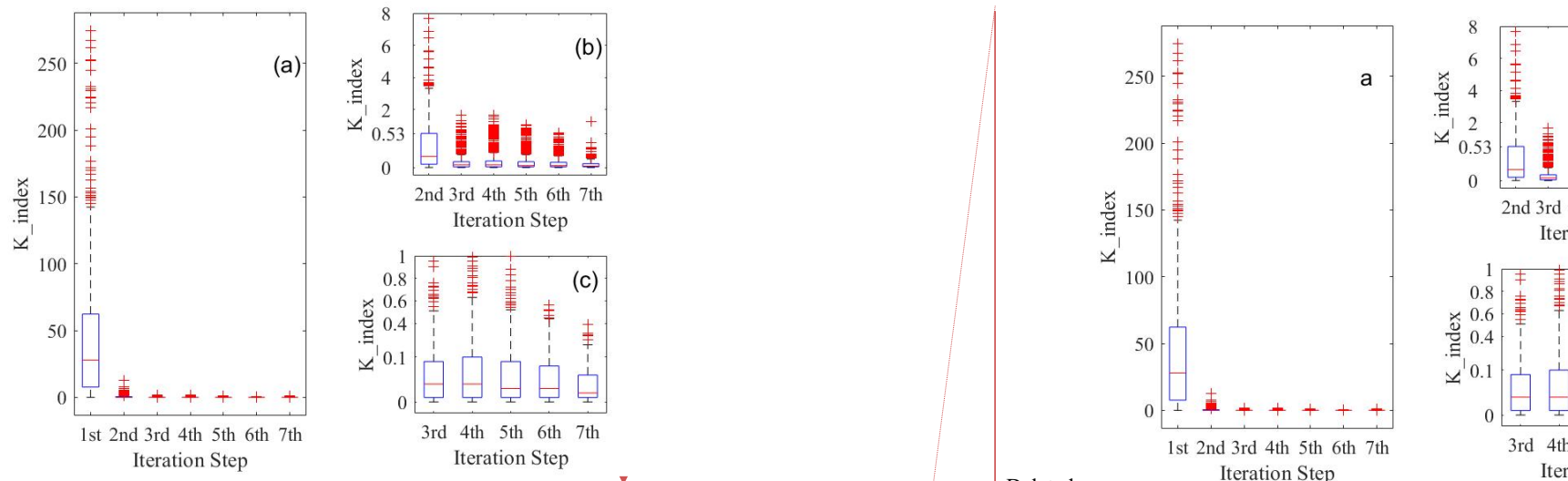


**Figure 3.** Box-and-whisker plots for  $K\_Index$  values at different iterations in the retrieval process of AERIOe. (a)  $K\_Index$  values calculated using 826 samples at iterations 1-7, (b) and (c) are the same as (a), but for iterations 2-7 and iterations 3-7, respectively. The boxes show upper-quartile, median (the red line through the middle of the box), and lower-quartile values for  $K\_Index$ . The whiskers extend to 1.5 times the interquartile range (IQR). Any outliers above or below the whiskers are plotted as red symbols '+'. Deleted: Deleted: Deleted: Deleted:

Fig. 3 shows the histogram of the  $K\_Index$  distribution for each iteration in the retrieval process, with the  $K\_Index$  values at each iteration calculated using the clear sky data for 2012. Since the climatological mean profile was used as the first-guess, which has a large deviation from the real atmospheric state, a larger value of  $K\_Index$  was demonstrated in the first step of the retrieval. The  $K\_Index$  value decreases significantly from the second iteration (see Fig. 3a), indicating that the adjustment of the iterative profile remains very small and that the retrieval process tends to be stable relative to the first iteration. As the retrieval proceeds, the iteration profile gradually approaches the truth, and the  $K\_Index$  box gradually shortens to below 0.5 (see Fig. 3b). Using this value as the threshold for  $K\_Index$ , most of the Jacobian after the second iteration does not need to be recalculated, and the retrieval time could be effectively reduced. However, the  $K\_Index$  in iteration 7 shows larger outliers, indicating that the instability of the retrieval algorithm increases when the  $\gamma$  factor decreases to 1. To reduce the impact of the Jacobian on the convergence of the algorithm, the threshold for the  $K\_Index$  after iteration 6 is set to 0.1 according to Fig. 3c, of which the  $K\_Index$  box at iteration 7 is within 0.1. It should be noted that the threshold of  $K\_Index$  used in the Fast AERIOe algorithm is dependent on the datasets used in the retrieval. They are presented 'as is' and are not intended to be directly applied by the reader. We encourage readers to develop their own indicator to reduce the recalculation of Jacobians based on the atmospheric profiles they intend to retrieve. Deleted: constituents

#### 4 Results and discussions

The simulated AERI radiation is used for retrieval to better analyze the performance of Fast AERIOe and eliminate the interference of other factors. An advantage of using synthetic observations is that the true atmospheric state is known, which

can be used to evaluate the retrieval accuracy. Second, the errors caused by parameters in the forward model, such as the deviation of trace gas content, the strength and temperature dependence of the water vapor continuum absorption, and the half-widths of absorption lines, could be eliminated (Maahn et al., 2020). Third, we can control the noise level in the synthetic measurement.

#### 225 4.1 Retrieval process

Examples of the Fast AERIOe retrieval using the simulated spectra at various iterations are shown in Fig. 4. These profiles represent the typical performance of each retrieval configuration at the SGP site. The entire retrieval process took 3.59 min with 7 iterations, in which only Jacobians of the first and second iterations were updated. The retrieved profiles converged quickly below 1 km, with little adjustment of the temperature and humidity profile following the first iteration. For the upper atmosphere above 1.5 km, the temperature and humidity profiles have a relatively large adjustment and gradually approach the radiosonde profile with the iterations. This feature of the Fast AERIOe retrieval process is very similar to AERIOe, which is determined by the information content of the AERI spectra. The information content is concentrated near the surface, which leads to a more rapid convergence in the lowest portions of the profile. The information content of the upper layer is lower, and as such, it is necessary to reduce the value of  $\gamma$  to introduce more observation information so that the retrieved profiles are refined to approach the radiosonde profile as the iterations are continued.

One advantage of the optimal estimation method remains that the posterior error covariance matrix of the solution  $\hat{\mathbf{S}}$  can be obtained to estimate the uncertainty of the retrieval results of each sample. The temperature and water vapor profile show a strong correlation for the correlation coefficient matrix of  $\mathbf{S}_a$  (see Fig. 5a and Fig. 5c), especially the temperature profile, which has a high correlation coefficient above 0.6 between any two layers because of the relatively stable vertical gradient of the temperature profile. The nondiagonal elements below 1 km in the correlation coefficient matrix of  $\hat{\mathbf{S}}$  results from Fast AERIOe show a much lower correlation than those of  $\mathbf{S}_a$  (see Fig. 5b and Fig. 5d), which means that the retrieved profiles in the lower atmosphere are dominated by AERI observations. However, with increasing height, the correlation of the area near the diagonal increases significantly. Therefore, the retrieval algorithm will rely more on the constraint of prior information at the upper layer of the PBL. The  $1-\sigma$  uncertainty lines, which are the square root of the diagonal of the covariance matrices for the prior (blue shaded area) and the posterior (black horizontal line) in Fig. 4, demonstrate that the retrieved profile has a much smaller uncertainty than the prior. Therefore, the Fast AERIOe algorithm can effectively reduce the impact of uncertainties in the first-guess profile on the retrieval results. As the height increases, the black horizontal line segment becomes longer for either the temperature profile or water vapor profile, indicating that the uncertainty in the retrieved profiles increases in the upper PBL.

Deleted: less

Deleted: -

Deleted: that

Deleted: the increase of

Deleted: is

Deleted: s

Deleted: for

Deleted: at

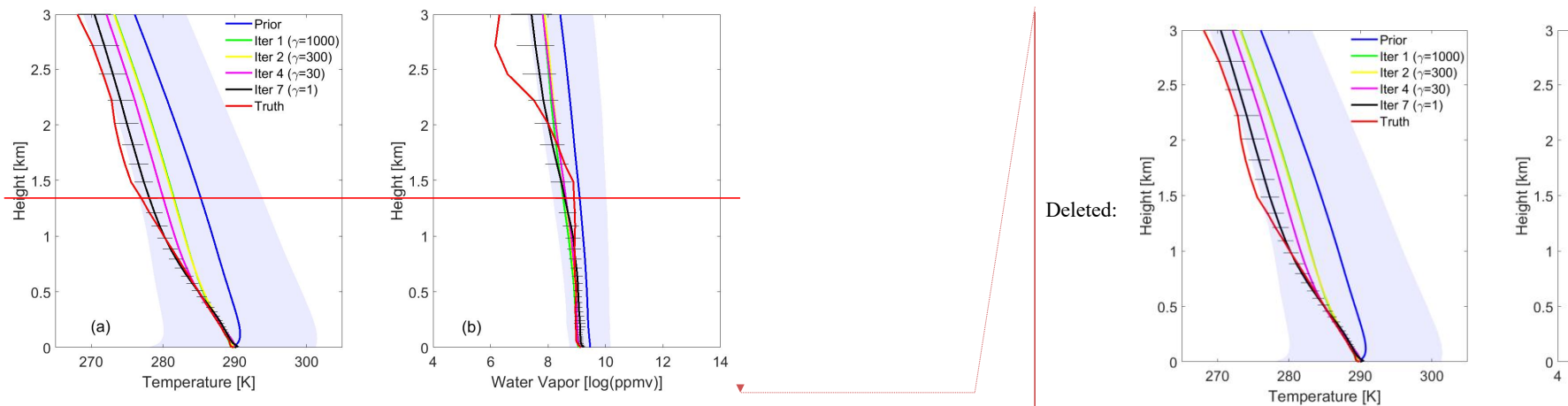


**Figure 4.** Retrieved (a) temperature and (b) water vapor profiles at various iterations from the simulated AERI observations, where the simulated observations were computed from a radiosonde (shown in red curves) launched at the SGP site at 11:30 UTC 20 Apr 2012. The prior mean profile (blue) was used as the first guess, and the blue-shaded area illustrates the 1- $\sigma$  uncertainties in the prior. The profiles at iterations 1, 2, and 7 are shown in solid blue, yellow, purple, and black (with 1- $\sigma$  error bars derived from  $\hat{S}$ ) lines, and the  $\gamma$  values were set to 1000, 300, 30 and 1 for the above iterations, respectively.

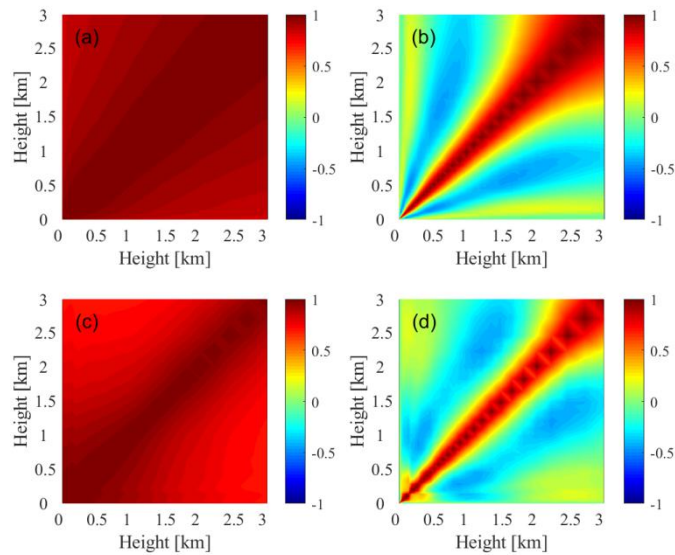


**Figure 5.** The level-to-level correlation of the prior (left) and posterior (right) for temperature (top row) and water vapor (bottom row) at 11:30 UTC 20 Apr 2012.

## 4.2 Performance

### 4.2.1 Retrieval time

Both AERIOe and Fast AERIOe algorithms were used to retrieve 826 groups of simulated AERI radiation data at SGP stations in 2012 to evaluate the retrieval performance of Fast AERIOe. The codes for both of the retrieval algorithms are written in MATLAB language and run on a Lenovo Aircross 510P computer, of which the CPU is Intel Core i7-7700 and the operating system is Ubuntu 14.04. To analyze the code timing of the retrieval algorithm, the code was divided into the following sections: preparation, iteration 1, iteration 2, iteration 3,... and iteration final. The preparation section mainly consists of atmosphere construction, observation vector construction and precalculated variable importation. The iteration sections

include the recalculation of  $\mathbf{K}$  and  $F(\mathbf{X})$  and the inversion using equation (1). Note that iteration 1 does not need to calculate  $\mathbf{K}$  and  $F(\mathbf{X})$  because the prior profile  $\mathbf{X}_a$  is fixed (mean value of the atmosphere), and the  $\mathbf{K}$  and  $F(\mathbf{X})$  associated with it are precalculated. The time consumed by each section was analyzed for both AERIOe and Fast AERIOe, and the results for an arbitrarily selected case are provided in Table 2. The recalculation of  $F(\mathbf{X})$  and  $\mathbf{K}$  consumed an immense amount of time in the retrieval process of AERIOe, and the latter is the most time-consuming section. Therefore, by reducing the recalculation of  $\mathbf{K}$ , the retrieval time of Fast AERIOe is greatly reduced compared to AERIOe.

**Table 2.** List of time consumption (units: s) by the AERIOe and Fast AERIOe sections. The sections denoted with superscript “\*” indicate that  $\mathbf{K}$  is not recalculated during the Fast AERIOe retrieval process.

Sections	AERIOe	Fast AERIOe
preparation	0.3	0.2
iteration 1 inversion	0.3	0.2
iteration 2 recalculation of $F(\mathbf{X})$	17.1	16.7
iteration 2 recalculation of $\mathbf{K}$	68.8	70.3
iteration 2 inversion	0.3	0.3
iteration 3 recalculation of $F(\mathbf{X})$	17.2	17.0
iteration 3 recalculation of $\mathbf{K}$	70.6	0.0
iteration 3 inversion	0.2	0.2
iteration 4 recalculation of $F(\mathbf{X})$	17.7	16.4
iteration 4 recalculation of $\mathbf{K}^*$	70.1	0.0
iteration 4 inversion	0.3	0.2
iteration 5 recalculation of $F(\mathbf{X})$	17.0	17.4
iteration 5 recalculation of $\mathbf{K}^*$	68.9	0.0
iteration 5 inversion	0.2	0.3
iteration 6 recalculation of $F(\mathbf{X})$	16.1	15.1
iteration 6 recalculation of $\mathbf{K}^*$	68.2	0.0
iteration 6 inversion	0.2	0.2
iteration final recalculation of $F(\mathbf{X})$	15.9	18.5
iteration final recalculation of $\mathbf{K}^*$	68.1	0.0
iteration final inversion	0.3	0.2

The average retrieval time of Fast AERIOe for the 826 cases used in the study is 3.7 min, which is more than 50% shorter than that of AERIOe, with an average retrieval time of 9.0 min, which is beyond the temporal resolution (approximately 8 min) of AERI observations. All of the AERIOe samples consumed more than 8 minutes, while only 10 cases exceeded the temporal resolution of AERI for Fast AERIOe algorithm. Note that the retrieval time is dependent on the computing platform and the method used to compute Jacobians and is not intended to be directly applied by the reader.

**Table 3.** The number of samples of different classes, which are classified according to  $K_{diff}$

Classification	$K_{diff}$	Sample Numbers
Class1	1	8

Deleted: -  
Deleted: for  
Deleted:  
Deleted: sections of  
Formatted: Font: Bold  
Deleted: 29  
Deleted: 2  
Deleted: 29  
Deleted: 2  
Deleted: 1  
Deleted: 69  
Deleted: 76  
Deleted: 27  
Deleted: 1  
Deleted: 27  
Deleted: 18  
Deleted: 4  
Deleted: 55  
Deleted: 0  
Deleted: 2  
Deleted: 2  
Deleted: 1  
Deleted: 36  
Deleted: 07  
Deleted: 0  
Deleted: 25  
Deleted: 1  
Deleted: 6  
Deleted: 97  
Deleted: 38  
Deleted: 3  
Deleted: 0  
Deleted: 1  
Deleted: 25

Class2	2	15
Class3	3	60
Class4	4	193
Class5	5	471
Class6	6	73
Class7	7	1

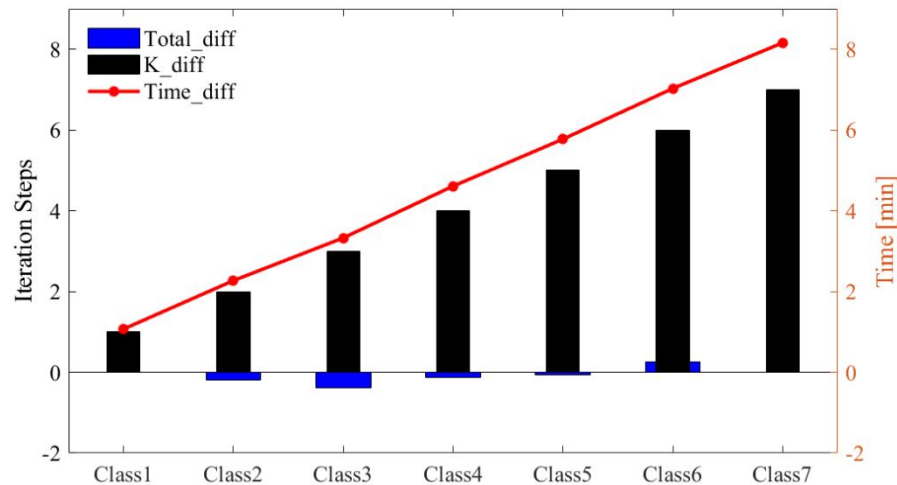


**Figure 6.** The distribution of  $K\_diff$ ,  $Total\_diff$  and  $Time\_diff$  with different classes.

In addition to, the recalculation of  $K$ , the retrieval time is also affected by the total iteration steps. Therefore, statistics of the average retrieval time difference ( $Time\_diff$  for short) caused by the  $K$  recalculation step difference ( $K\_diff$  for short) and average total iteration step difference ( $Total\_diff$  for short) are provided in this study. The retrieval samples are divided into 7 categories (shown in Table 3) in keeping with  $K\_diff$  between AERIOe and Fast AERIOe. On this basis,  $Time\_diff$  and  $Total\_diff$  between the two retrieval algorithms for various samples are calculated. As shown in Fig. 6, with an increase in  $K\_diff$ ,  $Time\_Diff$  also increased gradually, showing a strong positive correlation. Compared with  $K\_diff$ , the value of  $Total\_diff$  is very small, and its impact on the retrieval time is also minimal, only having a slight negative and positive effect on the  $Time\_diff$  of Class3 and Class6. Therefore, the improvement in the retrieval speed of Fast AERIOe is mainly due to the recalculation of Jacobians.

Deleted: Besides

Deleted: the

Deleted:

#### 4.2.2 Convergence characteristics

A total of 825 samples of the 826 datasets using the AERIOe algorithm achieved convergence, with the convergence rate reaching 99.9%. The Fast AERIOe algorithm has 815 groups of samples to achieve convergence, with the convergence rate reaching 98.7%, which is lower than that of AERIOe. Among the 11 sets of retrieval samples that did not achieve convergence, the  $K\_Index$  of most of them did not change much after the  $\gamma$  was dropped to 1, indicating that the subsequent iterations had little effect on the adjustment of the profiles, so the iterative profile corresponding to the minimum

Deleted:

Deleted: 88

*convergence\_index* could be taken as the retrieval results instead of criterion (2). Fig. 7a shows the comparison between the retrieved profiles from AERIOe using criteria (2) and Fast AERIOe using the new convergence criteria with 11 sets of nonconverged samples. The temperature profiles obtained by the two algorithms are virtually identical, with an R-square of 0.99. For the water vapor mixing ratio (WVMR), the introduction of the new convergence criteria reduces the value of R-square but still reaches 0.84, indicating that the two datasets still have a strong correlation. The above results indicate that the method of using the minimum *convergence\_index* to obtain the retrieval profiles is a reasonable and feasible method, as the Fast AERIOe algorithm cannot achieve convergence.

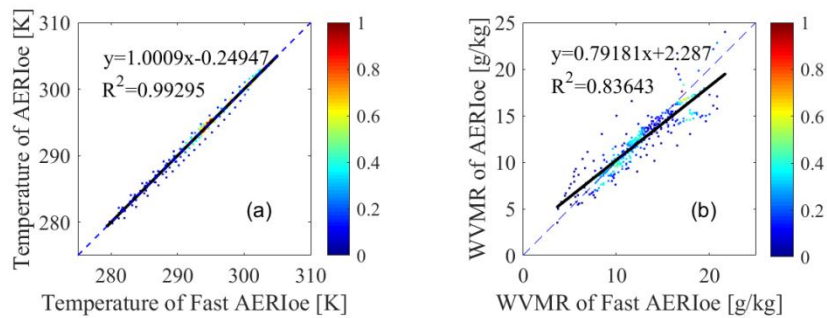


**Figure 7.** Scatter plots between the retrieval results of the nonconverged samples with AERIOe and Fast AERIOe. (a) Temperature profiles, (b) WVMR profiles.

#### 4.2.3 Accuracy

Traditional methods used to evaluate the accuracy of retrieved profiles against radiosondes compute the BIAS and root mean square error (RMSE), with the calculation formula as follows:

$$BIAS(i) = \frac{\sum_{j=1}^M (\mathbf{X}_{sonde}^{smooth}(i, j) - \mathbf{X}_{retrieval}(i, j))}{M}, \quad (8)$$

$$RMSE(i) = \sqrt{\frac{\sum_{j=1}^M (\mathbf{X}_{sonde}^{smooth}(i, j) - \mathbf{X}_{retrieval}(i, j))^2}{M}}, \quad (9)$$

where  $i$  and  $j$  represent the serial numbers of vertical stratification and samples, respectively, with  $M$  being the number of samples.  $\mathbf{X}_{retrieval}$  is defined as retrieved profiles, and  $\mathbf{X}_{sonde}^{smooth}$  is radiosonde observations that are smoothed with the averaging kernel  $\mathbf{A}$  by the following multiplication to reduce the vertical representativeness errors:

$$\mathbf{X}_{sonde}^{smoothed} = \mathbf{A}(\mathbf{X}_{sonde} - \mathbf{X}_a) + \mathbf{X}_a, \quad (10)$$

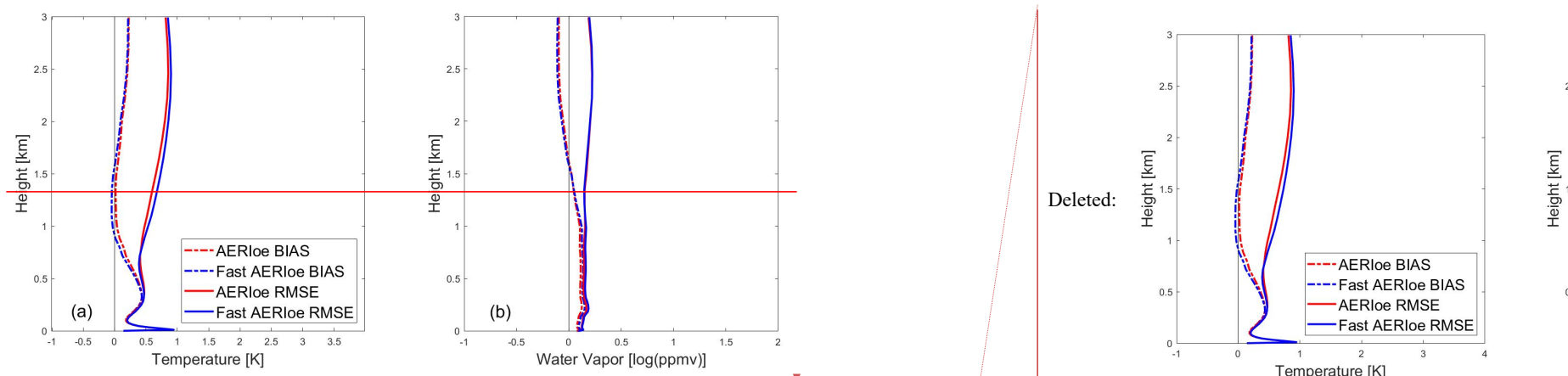


**Figure 8.** Bias (solid curves) and RMSE (dashed curves) profiles for clear-sky comparisons of the AERIoe (red curves) and Fast AERIoe (blue curves) retrievals with radiosondes. (a) Temperature profile, (b) Water Vapor profiles.

The BIAS and RMSE of AERIoe and Fast AERIoe are calculated for 826 sets of samples using the above equations within the altitude range of 0-3 km, and the results are shown in Fig. 8. The temperature profile below 1.0 km and the water vapor profile below 1.5 km have obvious positive deviations, with the maximum deviations reaching 1.0 K and 0.2 log(ppmv), respectively. However, the BIAS and RMSE at the bottom are significantly reduced due to the constraint of the surface observations, indicating that the introduction of surface meteorological observation data in the observation vector has an obvious positive effect. The Fast AERIoe retrieved temperature profiles show a negative deviation of 0.05 K between 1.0 km and 1.5 km and a maximum increase in RMSE within 0.08 K above 1.0 km when compared with AERIoe. For the water vapor profile, the BIAS and RMSE profiles of Fast AERIoe are in good agreement with AERIoe, except for a maximum increase in BIAS within 0.03 log(ppmv) below 1.0 km. When considering the magnitude of the temperature (roughly on the order of 300 K) and water vapor (roughly on the order of 5-10 log(ppmv)) profiles, the differences between the retrieved profiles are negligible, indicating that the retrieval results of Fast AERIoe are comparable to those of AERIoe.

The comparison of the profiles retrieved by the two algorithms can be demonstrated more clearly by the modified Taylor plots (Turner and Löhnert, 2014), which are used to evaluate how well each retrieved profile can capture the vertical shapes of its true profile, as BIAS and RMSE can only describe the average accuracy of the whole dataset at each height. These Taylor diagrams show Pearson's correlation coefficient between two datasets on the y-axis and the ratio of the standard deviation on the x-axis. Each retrieval/sonde pair is used to derive the correlation coefficient ( $r$ ) from Eq. (11) and the ratio of the standard deviations from Eq.(12), both are used by Turner and Löhnert (2014).

$$r = \frac{\frac{1}{N} \sum_{z=0}^{z=h} [s(z) - \bar{s}] [a(z) - \bar{a}]}{\sigma_s \sigma_a}, \quad (11)$$

$$SDR = \sigma_a / \sigma_s, \quad (12)$$

Within the equations,  $s(z)$  and  $a(z)$  are defined as the radiosonde observations and retrieved profiles between 0 and 3 km, and  $(\bar{s}, \bar{a})$  and  $(\sigma_s, \sigma_a)$  are the mean values and standard deviations at the same height range.

Retrievals that have a correlation coefficient of 1 and a standard deviation ratio (SDR) of 1 mean that the two datasets match perfectly. Fig. 9a and Fig. 9b show these plots for the clear-sky AERIoe and fast AERIoe retrievals. For the temperature retrievals, both the Fast AERIoe and the AERIoe perform well, with 90 percent of correlation coefficients above 0.9 and the intersection of the arms close to 1. Fig. 9b shows that retrieving the water vapor structure is much more difficult with both algorithms; the spread in the correlation coefficient and SDR are much larger for water vapor than for temperature. Most of the blue and red symbols 'x' in Fig. 9, which indicate the scores for the individual profiles of the two algorithms, are close to each other for both the temperature and water vapor profiles. Therefore, the modified Taylor plots also confirm the conclusion that the retrieval results of the AERIoe and Fast AERIoe algorithms are comparable.

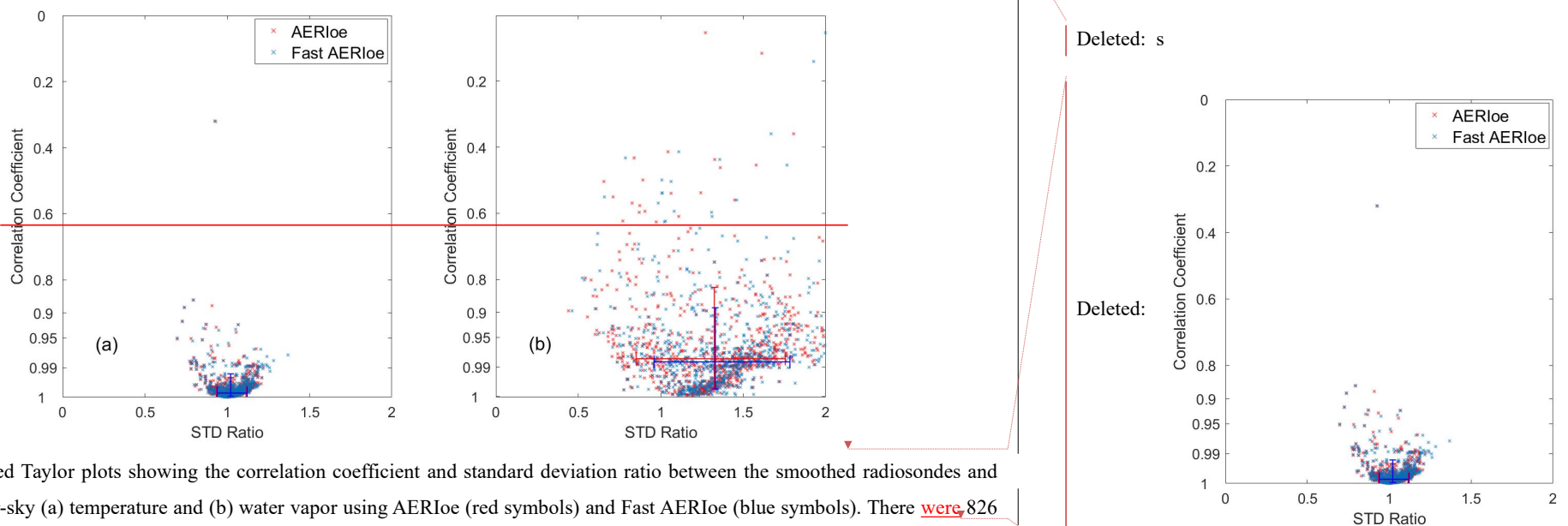


**Figure 9.** Modified Taylor plots showing the correlation coefficient and standard deviation ratio between the smoothed radiosondes and the retrieved clear-sky (a) temperature and (b) water vapor using AERIoe (red symbols) and Fast AERIoe (blue symbols). There were 826 cases from the SGP site within 2012. Each symbol indicates the score for an individual profile. The arms of the plotted crosses span the 10th–90th percentiles for the correlation coefficient (vertical arms) and the standard deviation ratio (horizontal arms).

### 4.3 Real observations

Since the clouds overhead have a significant influence on the infrared spectra, the primary problem is how to screen clear-sky samples when using the measured AERI data to retrieve the temperature and humidity profile. The contribution of clouds to infrared radiation not only interferes with the inversion of temperature and humidity profiles but also provides technical means for obtaining cloud macro parameters (Liu et al., 2022). Fig. 10 shows the AERI observed spectrum under cloudy and clear sky conditions. The AERI observations under the two conditions remain highly different, indicating that the AERI observed spectrum can be adopted directly to determine whether clouds or clear skies are present. To establish an accurate cloud recognition model, we adopted the cloud fraction data obtained from the all-sky image at the same site as the



label for training, where the sample with a cloud fraction less than 30% is marked as 0, indicating clear sky, while the sample with a cloud fraction greater than 30% is marked as 1, indicating that there is cloud over head. Using the above-mentioned method, the cloud fraction of the all-sky image from March to May 2010 was labeled and temporally matched with the AERI observed radiance to form a training dataset, based on which a cloud recognition model was established by training the back propagation (BP) neural network, with the final cross-validation accuracy reaching 94.3%. Compared with the recognition method by radiosonde, the BP cloud recognition model greatly improves the discrimination accuracy without requiring additional detection equipment. The BP cloud recognition model was applied to the 178 groups of AERI observations collected on October 21, 2012, with 168 groups of clear sky samples screened in total.

Deleted:

Deleted:

Deleted: has

Deleted: d

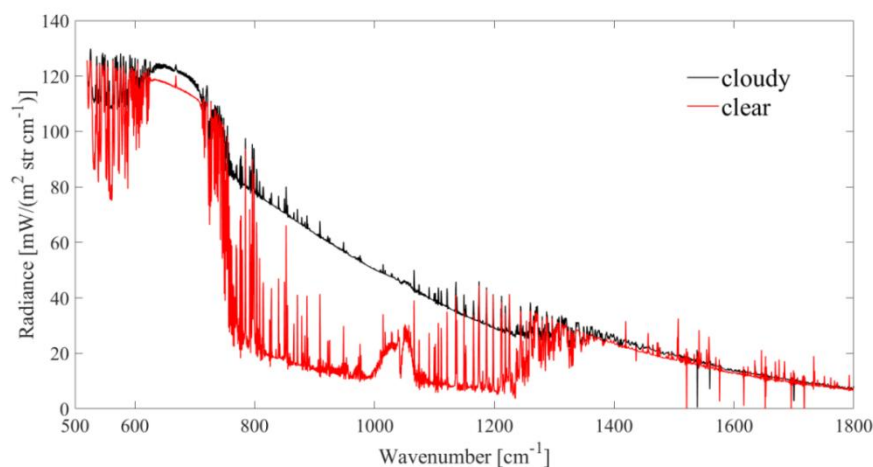


Figure 10. AERI observations in clear and cloudy sky conditions.

Benefiting from good retrieval accuracy and high temporal resolution, AERI instruments can be used to monitor thermodynamic temporal structures that may not be resolved by infrequent radiosonde launches. Fig. 11 shows the time–height cross sections of the temperature and WVMR profiles derived from the Fast AERIOe retrievals. Fig. 11 shows that the AERI resolved the temperature inversion prior to approximately 15:00 UTC, and the height of the inversion layer gradually increased over time. After 15:00 UTC, the temperature near the surface increases significantly, accompanied by the disappearance of the inversion layer. From the comparisons with radiosonde profiles shown in Fig. 12, the retrieval results of Fast AERIOe are well matched with radiosonde profiles, especially the temperature profiles, which demonstrates the ability of the algorithm to resolve the inversion layer.

Deleted: It can be seen from

Deleted: rising

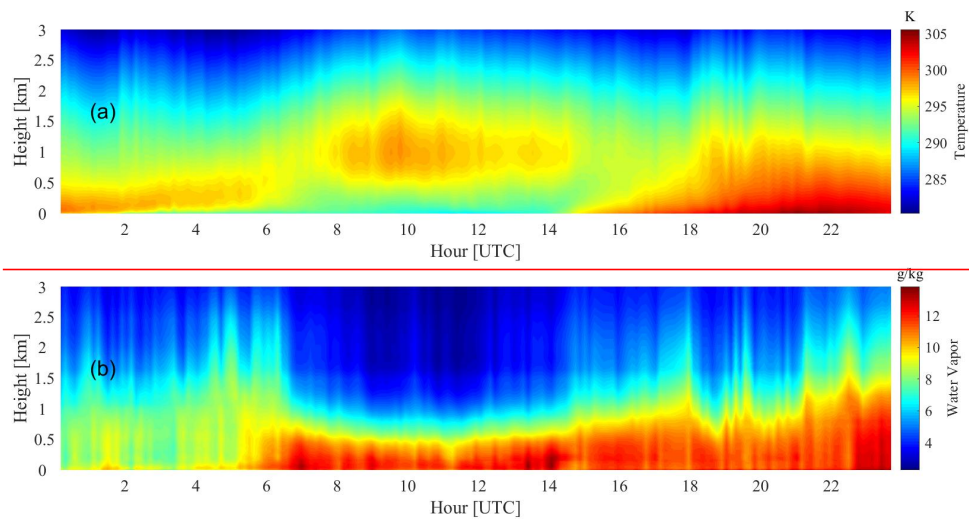


Figure 11. Time-height cross sections of temperature (a) and water vapor (b) on Oct. 21, 2012.

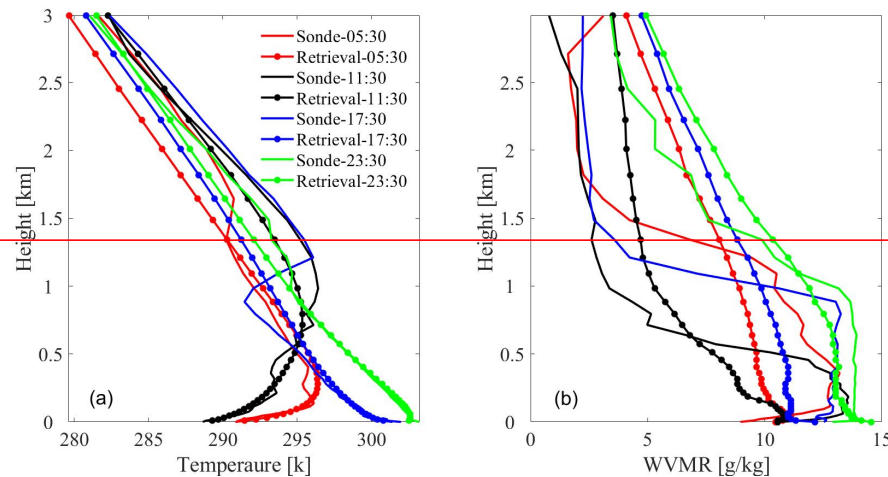
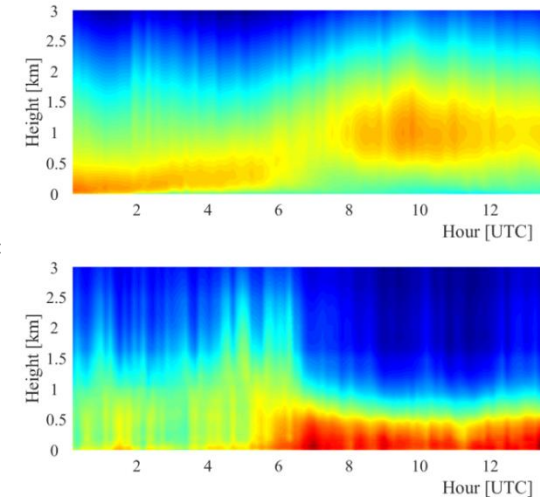


Figure 12. Comparisons between retrieved thermodynamic profiles and the coincident radiosonde profiles at 05:30 UTC, 11:30 UTC, 17:30 UTC and 23:30 UTC on Oct. 21, 2012. (a) Temperature profiles, (b) WVMR profiles.

## 5 Conclusions

The AERIOe algorithm retrieves atmospheric temperature and humidity profiles using the optimal estimation framework, which can make full use of information in the infrared spectrum and give the uncertainty of each retrieval result. AERIOe reduces the dependence on the first-guess profile by introducing regularization parameters, but it also requires more iterative steps, which increases the calculation amount and retrieval time of the algorithm. In this paper, a fast retrieval method called Fast AERIOe is established by adaptively recalculating the Jacobians in the retrieval process of AERIOe. Based on the statistical comparison of the two methods (AERIOe and Fast AERIOe) with radiosonde observations, the retrieval performance of Fast AERIOe is summarized as follows:

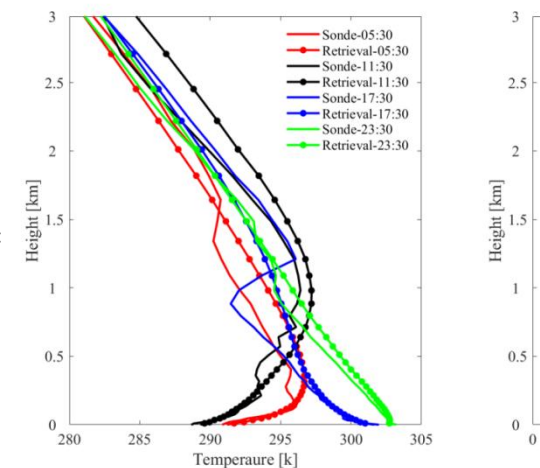
1. The retrieval speed of the Fast AERIOe is significantly improved compared with AERIOe while keeping the parameters of the computing platform unchanged, with the average retrieval time reduced by more than 50%. The



Deleted:

Deleted: top

Deleted: bottom



Deleted:

Deleted: Left

Deleted: right

Deleted: on the basis of

Deleted: algorithm

Deleted: s

Deleted: at the same time,

Deleted: on the basis of AERIOe

Deleted: are

395 temperature and water vapor profiles derived from Fast AERIoe ~~are~~ almost unchanged compared with AERIoe, illustrating that the retrieval results of Fast AERIoe ~~are~~ comparable to ~~those~~ of AERIoe. ~~The deep retrieval architecture is able to extract highly nonlinear features from the AERI observations, which shows a better inversion capability than the existing statistical methods (Yang et al., 2023), albeit with the lack of the radiative transfer process. Therefore, the combination of AERIoe and deep learning can improve the accuracy of AERI for retrieving temperature and humidity profiles.~~

Deleted: is  
Deleted: is  
Deleted: that

400 2. ~~For the convergence characteristics, 825 out of 826 samples adopt~~ing AERIoe meet the convergence criterion, while the sample adopt~~ing~~ Fast AERIoe converg~~es~~ over 98% of the time. The method of recalculating Jacobians in Fast AERIoe slightly reduces the convergence of the retrieval algorithm. Despite this, the Fast AERIoe algorithm ~~has~~ demonstrated the ability to retrieve reliable temperature and water vapor profiles more quickly, which is fast enough for real-time processing.

Deleted: As f  
Deleted: ed  
Deleted: s  
Deleted: ed

405 3. When Fast AERIoe is adopted to measure ~~the~~ AERI spectrum, a cloud recognition model without additional detection equipment is established based on the BP neural network algorithm to remove cloudy-sky cases. Compared with the commonly used cloud recognition method by radiosonde observations, the BP cloud recognition model has greatly improved the discrimination accuracy. It should be noted that the hyperspectra under the two weather conditions of clear sky with high humidity and few clouds are relatively close, while the above two weather conditions are far from further distinguished when building the BP cloud recognition model, which may reduce the discriminative accuracy of the model. ~~Furthermore, the cloud base height (CBH) also contributes to AERI radiation (Ye et al., 2022), and adding CBH to the recognition model helps to improve the accuracy of the model.~~

Deleted: ed  
Deleted: have  
Deleted: the  
Deleted: d

410 A single instrument always has some defects ~~in~~ vertical coverage, vertical resolution, temporal resolution and accuracy in obtaining the vertical distribution of atmospheric constituents (Barrera-Verdejo et al., 2016). The combination of multiple remote sensing devices in an optimal retrieval algorithm can overcome the shortcomings of a single device, making full use of each measurement to achieve the purpose of enhancing their benefits. However, the increase in observation equipment will inevitably lead to more complex calculations of the forward model and Jacobian, which will lead to a significant increase in the amount of calculation and retrieval time. Therefore, it is particularly necessary to carry out research on fast retrieval in ~~the~~ case of joint retrieval. Apart from the influence of the Jacobian on the retrieval time, so does the number of iterations required by the retrieval algorithm, which is dominated by the regularization parameter. Future work will focus on the application of Fast AERIoe in the combination of different observations and the selection of regularization parameters to permit the retrieval algorithm to converge more efficiently.

Deleted: at  
Deleted: the

425 *Data availability.* The data used in the manuscript (including AERI, radiosonde, etc) are available from the ARM Data Archive (<https://adc.arm.gov/discovery/#/>, accessed on 19 January 2022). The code for recalculating Jacobians ~~is~~ not publicly available at this time but may be obtained from the authors upon reasonable request.

Deleted: are

*Author contributions.* LL, BY and WH determined the main goal of this study. WH developed the approach, analyzed the data, and visualized the results of the experiments. LL prepared the paper with contributions from all coauthors. SH acquired funding and edited the paper. WL and WY prepared the various datasets. ZL and XY provided guidance on algorithmic procedures. All the coauthors reviewed the paper.

Deleted: -

Deleted:

Deleted: -

*Competing interests.* The contact author has declared that none of the authors has any competing interests.

*Acknowledgments.* The authors thank the U. S. Department of Energy (DOE) Atmospheric Radiation Measurement (ARM) Program for providing meteorological data online for free. The authors are deeply grateful to Atmospheric and Environmental Research (AER) Inc. for providing the LBLRTM codes online for free.

*Financial support.* This work is supported by the National Natural Science Foundation of China (Grant No. 42175154 and Grant No. 62105367) and Natural Science Foundation of Hunan Province (Grant No. 2020JJ4662).

## References

Barrera-Verdejo, M., Crewell, S., Löhnert, U., Orlandi, E., and Di Girolamo, P.: Ground-based lidar and microwave radiometry synergy for high vertical resolution absolute humidity profiling, *Atmospheric Measurement Techniques*, 9, 4013-4028, <https://doi.org/10.5194/amt-9-4013-2016>, 2016.

Barthlott, S., Schneider, M., Hase, F., Blumenstock, T., Kiel, M., Dubravica, D., García, O. E., Sepúlveda, E., Mengistu Tsidu, G., Takele Kenea, S., Grutter, M., Plaza-Medina, E. F., Stremme, W., Strong, K., Weaver, D., Palm, M., Warneke, T., Notholt, J., Mahieu, E., Servais, C., Jones, N., Griffith, D. W. T., Smale, D., and Robinson, J.: Tropospheric water vapour isotopologue data ( H<sub>2</sub>16O, H<sub>2</sub>18O, and HD16O) as obtained from NDACC/FTIR solar absorption spectra, *Earth Syst. Sci. Data*, 9, 15-29, <https://doi.org/10.5194/essd-9-15-2017>, 2017.

Blumberg, W., Wagner, T., Turner, D., and Correia Jr, J.: Quantifying the accuracy and uncertainty of diurnal thermodynamic profiles and convection indices derived from the Atmospheric Emitted Radiance Interferometer, *Journal of Applied Meteorology and Climatology*, 56, 2747-2766, <https://doi.org/10.1175/JAMC-D-17-0036.1>, 2017.

- Blumberg, W. G., Turner, D. D., Löhnert, U., and Castleberry, S.: Ground-Based Temperature and Humidity Profiling Using Spectral Infrared and Microwave Observations. Part II: Actual Retrieval Performance in Clear-Sky and Cloudy  
455 Conditions, Journal of Applied Meteorology and Climatology, 54, 2305-2319,  
<https://doi.org/10.1175/jamc-d-15-0005.1>, 2015.
- Cimini, D., Westwater, E. R., and Gasiewski, A. J.: Temperature and Humidity Profiling in the Arctic Using Ground-Based Millimeter-Wave Radiometry and 1DVAR, IEEE Transactions on Geoscience and Remote Sensing, 48,  
1381-1388, <https://doi.org/10.1109/TGRS.2009.2030500>, 2010.
- 460 De Mazière, M., Thompson, A. M., Kurylo, M. J., Wild, J. D., Bernhard, G., Blumenstock, T., Braathen, G. O.,  
Hannigan, J. W., Lambert, J. C., Leblanc, T., McGee, T. J., Nedoluha, G., Petropavlovskikh, I., Seckmeyer, G., Simon,  
P. C., Steinbrecht, W., and Strahan, S. E.: The Network for the Detection of Atmospheric Composition Change  
(NDACC): history, status and perspectives, Atmos. Chem. Phys., 18, 4935-4964,  
<https://doi.org/10.5194/acp-18-4935-2018>, 2018.
- 465 Ellingson, R. G., Cess, R. D., and Potter, G. L.: The atmospheric radiation measurement program: Prelude,  
Meteorological Monographs, 57, 1.1-1.9, <https://doi.org/10.1175/AMSMONOGRAPHS-D-15-0029.1>, 2016.
- Feltz, W. F., Smith, W. L., Knuteson, R. O., Revercomb, H. E., Woolf, H. M., and Howell, H. B.: Meteorological  
applications of temperature and water vapor retrievals from the ground-based Atmospheric Emitted Radiance  
Interferometer (AERI), Journal of Applied Meteorology, 37, 857-875,  
470 [https://doi.org/10.1175/1520-0450\(1998\)037<0857:MAOTAW>2.0.CO;2](https://doi.org/10.1175/1520-0450(1998)037<0857:MAOTAW>2.0.CO;2), 1998.
- Gardiner, T., Forbes, A., de Mazière, M., Vigouroux, C., Mahieu, E., Demoulin, P., Velazco, V., Notholt, J.,  
Blumenstock, T., Hase, F., Kramer, I., Sussmann, R., Stremme, W., Mellqvist, J., Strandberg, A., Ellingsen, K., and  
Gauss, M.: Trend analysis of greenhouse gases over Europe measured by a network of ground-based remote FTIR  
instruments, Atmos. Chem. Phys., 8, 6719-6727, <https://doi.org/10.5194/acp-8-6719-2008>, 2008.
- 475 Geerts, B., Raymond, D. J., Grubišić, V., Davis, C. A., Barth, M. C., Detwiler, A., Klein, P. M., Lee, W.-C., Markowski,

P. M., Mullendore, G. L., and Moore, J. A.: Recommendations for In Situ and Remote Sensing Capabilities in Atmospheric Convection and Turbulence, *Bulletin of the American Meteorological Society*, 99, 2463-2470, <https://doi.org/10.1175/bams-d-17-0310.1>, 2018.

480 Kain, J. S., Coniglio, M. C., Correia, J., Clark, A. J., Marsh, P. T., Ziegler, C. L., Lakshmanan, V., Miller, S. D., Dembek, S. R., and Weiss, S. J.: A feasibility study for probabilistic convection initiation forecasts based on explicit numerical guidance, *Bulletin of the American Meteorological Society*, 94, 1213-1225, <https://doi.org/10.1175/BAMS-D-11-00264.1>, 2013.

Kiel, M., Wunch, D., Wennberg, P. O., Toon, G. C., Hase, F., and Blumenstock, T.: Improved retrieval of gas abundances from near-infrared solar FTIR spectra measured at the Karlsruhe TCCON station, *Atmos. Meas. Tech.*, 9, 485 669-682, <https://doi.org/10.5194/amt-9-669-2016>, 2016.

Knuteson, R., Revercomb, H., Best, F., Ciganovich, N., Dedecker, R., Dirx, T., Ellington, S., Feltz, W., Garcia, R., and Howell, H.: Atmospheric emitted radiance interferometer. Part I: Instrument design, *Journal of Atmospheric and Oceanic Technology*, 21, 1763-1776, <https://doi.org/10.1175/JTECH-1662.1>, 2004.

Li, J., Wang, P., Han, H., Li, J., and Zheng, J.: On the assimilation of satellite sounder data in cloudy skies in numerical 490 weather prediction models, *Journal of Meteorological Research*, 30, 169-182, <https://doi.org/10.1007/s13351-016-5114-2>, 2016.

Liu, L., Ye, J., Li, S., Hu, S., and Wang, Q.: A novel machine learning algorithm for cloud detection using aeri measurement data, *Remote Sensing*, 14, 2589, <https://doi.org/https://doi.org/10.3390/rs14112589>, 2022.

Maahn, M., Turner, D. D., Löhnert, U., Posselt, D. J., Ebell, K., Mace, G. G., and Comstock, J. M.: Optimal Estimation 495 Retrievals and Their Uncertainties: What Every Atmospheric Scientist Should Know, *Bulletin of the American Meteorological Society*, 101, E1512-E1523, <https://doi.org/10.1175/bams-d-19-0027.1>, 2020.

Revercomb, H. E., Turner, D. D., Tobin, D. C., Knuteson, R. O., Feltz, W. F., Barnard, J., Bösenberg, J., Clough, S., Cook, D., Ferrare, R., Goldsmith, J., Gutman, S., Halthore, R., Lesht, B., Liljegren, J., Linné, H., Michalsky, J., Morris,

V., Porch, W., Richardson, S., Schmid, B., Splitt, M., Van Hove, T., Westwater, E., and Whiteman, D.: The Arm  
500 Program's Water Vapor Intensive Observation Periods: Overview, Initial Accomplishments, and Future Challenges,  
Bulletin of the American Meteorological Society, 84, 217-236, <https://doi.org/10.1175/bams-84-2-217>, 2003.

Rodgers, C. D.: Information content and optimisation of high spectral resolution remote measurements, Advances in  
Space Research, 21, 361-367, [https://doi.org/10.1016/S0273-1177\(97\)00915-0](https://doi.org/10.1016/S0273-1177(97)00915-0), 1998.

Rodgers, C. D.: Inverse methods for atmospheric sounding: theory and practice, World scientific, 119-120 pp.,  
505 ISBN9814498688, 2000.

Romine, G. S., Schwartz, C. S., Snyder, C., Anderson, J. L., and Weisman, M. L.: Model bias in a continuously cycled  
assimilation system and its influence on convection-permitting forecasts, Monthly weather review, 141, 1263-1284,  
<https://doi.org/10.1175/MWR-D-12-00112.1>, 2013.

Rowe, P. M., Walden, V. P., and Warren, S. G.: Measurements of the foreign-broadened continuum of water vapor in  
510 the 6.3  $\mu\text{m}$  band at  $-30\text{ }^{\circ}\text{C}$ , Applied Optics, 45, 4366-4382, <https://doi.org/10.1364/AO.45.004366>, 2006.

Schneider, M. and Hase, F.: Ground-based FTIR water vapour profile analyses, Atmospheric Measurement Techniques,  
2, 609-619, <https://doi.org/https://doi.org/10.5194/amt-2-609-2009>, 2009.

Schneider, M., Hase, F., and Blumenstock, T.: Ground-based remote sensing of HDO/H<sub>2</sub>O ratio profiles: introduction  
and validation of an innovative retrieval approach, Atmospheric Chemistry and Physics, 6, 4705-4722,  
515 <https://doi.org/https://doi.org/10.5194/acp-6-4705-2006>, 2006a.

Schneider, M., Hase, F., and Blumenstock, T.: Water vapour profiles by ground-based FTIR spectroscopy: study for an  
optimised retrieval and its validation, Atmospheric Chemistry and Physics, 6, 811-830,  
<https://doi.org/10.5194/acp-6-811-2006>, 2006b.

Sisterson, D., Pepler, R., Cress, T., Lamb, P., and Turner, D.: The ARM southern great plains (SGP) site,  
520 Meteorological Monographs, 57, 6.1-6.14, <https://doi.org/10.1175/AMSMONOGRAPHS-D-16-0004.1>, 2016.

Smith, W. L., Feltz, W. F., Knuteson, R. O., Revercomb, H. E., Woolf, H. M., and Howell, H. B.: The retrieval of

planetary boundary layer structure using ground-based infrared spectral radiance measurements, *Journal of Atmospheric and Oceanic Technology*, 16, 323-333, [https://doi.org/10.1175/1520-0426\(1999\)016<0323:TROPBL>2.0.CO;2](https://doi.org/10.1175/1520-0426(1999)016<0323:TROPBL>2.0.CO;2), 1999.

525 Turner, D. D. and Blumberg, W. G.: Improvements to the AERIOe Thermodynamic Profile Retrieval Algorithm, *IEEE Journal of Selected Topics in Applied Earth Observations and Remote Sensing*, 12, 1339-1354, <https://doi.org/10.1109/JSTARS.2018.2874968>, 2019.

Turner, D. D. and Löhnert, U.: Information Content and Uncertainties in Thermodynamic Profiles and Liquid Cloud Properties Retrieved from the Ground-Based Atmospheric Emitted Radiance Interferometer (AERI), *Journal of Applied Meteorology and Climatology*, 53, 752-771, <https://doi.org/10.1175/jamc-d-13-0126.1>, 2014.

530 Turner, D. D. and Löhnert, U.: Ground-based temperature and humidity profiling: combining active and passive remote sensors, *Atmospheric Measurement Techniques*, 14, 3033-3048, <https://doi.org/10.5194/amt-14-3033-2021>, 2021.

Turner, D. D., Feltz, W. F., and Ferrare, R. A.: Continuous water vapor profiles from operational ground-based active and passive remote sensors, *Bulletin of the American Meteorological Society*, 81, 1301-1318, [https://doi.org/10.1175/1520-0477\(2000\)081<1301:CWBPFO>2.3.CO;2](https://doi.org/10.1175/1520-0477(2000)081<1301:CWBPFO>2.3.CO;2), 2000.

Turner, D. D., Mlawer, E. J., and Revercomb, H. E.: Water Vapor Observations in the ARM Program, *Meteorological Monographs*, 57, 13.11-13.18, <https://doi.org/10.1175/amsmonographs-d-15-0025.1>, 2016.

Viatte, C., Strong, K., Walker, K. A., and Drummond, J. R.: Five years of CO, HCN, C<sub>2</sub>H<sub>6</sub>, C<sub>2</sub>H<sub>2</sub>, CH<sub>3</sub>OH, HCOOH and H<sub>2</sub>CO total columns measured in the Canadian high Arctic, *Atmos. Meas. Tech.*, 7, 1547-1570, <https://doi.org/10.5194/amt-7-1547-2014>, 2014.

Wagner, T. J., Klein, P. M., and Turner, D. D.: A new generation of ground-based mobile platforms for active and passive profiling of the boundary layer, *Bulletin of the American Meteorological Society*, 100, 137-153, <https://doi.org/10.1175/BAMS-D-17-0165.1>, 2019.



- 545 Wakefield, R. A., Turner, D. D., and Basara, J. B.: Evaluation of a Land–Atmosphere Coupling Metric Computed from a Ground-Based Infrared Interferometer, *Journal of Hydrometeorology*, 22, 2073-2087, <https://doi.org/10.1175/jhm-d-20-0303.1>, 2021.
- Yang, J. and Min, Q.: Retrieval of atmospheric profiles in the New York State Mesonet using one-dimensional variational algorithm, *Journal of Geophysical Research: Atmospheres*, 123, 7563-7575, 550 <https://doi.org/10.1029/2018JD028272>, 2018.
- Yang, W., Liu, L., Deng, W., Huang, W., Ye, J., and Hu, S.: Deep Retrieval Architecture of Temperature and Humidity Profiles from Ground-Based Infrared Hyperspectral Spectrometer, *Remote Sensing*, 15, 2320, <https://doi.org/https://doi.org/10.3390/rs15092320>, 2023.
- Ye, J., Liu, L., Yang, W., and Ren, H.: Using Artificial Neural Networks to Estimate Cloud-Base Height From AERI 555 Measurement Data, *IEEE Geoscience and Remote Sensing Letters*, 19, 1-5, <https://doi.org/10.1109/LGRS.2022.3182473>, 2022.
- Yin, H., Sun, Y., Liu, C., Wang, W., Shan, C., and Zha, L.: Remote Sensing of Atmospheric Hydrogen Fluoride (HF) over Hefei, China with Ground-Based High-Resolution Fourier Transform Infrared (FTIR) Spectrometry, *Remote Sensing*, 13, 791, <https://doi.org/https://doi.org/10.3390/rs13040791>, 2021a.
- 560 Yin, H., Sun, Y., Wang, W., Shan, C., Tian, Y., and Liu, C.: Ground-based high-resolution remote sensing of sulphur hexafluoride (SF<sub>6</sub>) over Hefei, China: characterization, optical misalignment, influence, and variability, *Optics Express*, 29, 34051-34065, <https://doi.org/10.1364/OE.440193>, 2021b.
- Yin, H., Sun, Y., Liu, C., Lu, X., Smale, D., Blumenstock, T., Nagahama, T., Wang, W., Tian, Y., Hu, Q., Shan, C., Zhang, H., and Liu, J.: Ground-based FTIR observation of hydrogen chloride (HCl) over Hefei, China, and 565 comparisons with GEOS-Chem model data and other ground-based FTIR stations data, *Optics Express*, 28, 8041-8055, <https://doi.org/10.1364/OE.384377>, 2020.
- Zhou, M., Langerock, B., Vigouroux, C., Sha, M. K., Ramonet, M., Delmotte, M., Mahieu, E., Bader, W., Hermans, C.,

Kumps, N., Metzger, J. M., Duflot, V., Wang, Z., Palm, M., and De Mazière, M.: Atmospheric CO and CH<sub>4</sub> time series and seasonal variations on Reunion Island from ground-based in situ and FTIR (NDACC and TCCON) measurements,

570 Atmos. Chem. Phys., 18, 13881-13901, <https://doi.org/10.5194/acp-18-13881-2018>, 2018.